

PAPER

Impact of Labeling Inaccuracy and Image Noise on Tooth Segmentation in Panoramic Radiographs using Federated, Centralized and Local Learning

Johan Andreas Balle Rubak^{1,*}, Khuram Naveed¹, Sanyam Jain¹, Lukas Esterle², Alexandros Iosifidis³ and Ruben Pauwels¹

¹Department of Dentistry and Oral Health, Aarhus University, Vennelyst Boulevard 9, 8000, Aarhus, Denmark, ²Department of Electrical- and Computer Engineering, Aarhus University, Finlandsgade 22, 8200, Aarhus, Denmark and ³Faculty of Information Technology and Communications Sciences, Tampere University, Kalevantie 4, 33100, Tampere, Finland

*Corresponding author. joru@dent.au.dk

Abstract

Objectives: Federated learning (FL) may mitigate privacy constraints, heterogeneous data quality, and inconsistent labeling in dental diagnostic AI. We compared FL with centralized (CL) and local learning (LL) for tooth segmentation in panoramic radiographs across multiple data corruption scenarios.

Methods: An Attention U-Net was trained on 2066 radiographs from six institutions across four settings: baseline (unaltered data); label manipulation (dilated/missing annotations); image-quality manipulation (additive Gaussian noise); and exclusion of a faulty client with corrupted data. FL was implemented via the Flower AI framework. Per-client training- and validation loss trajectories were monitored for anomaly detection and a set of metrics (Dice, IoU, HD, HD95 and ASSD) was evaluated on a hold-out test set. From these metrics significance results were reported through Wilcoxon signed-rank test. CL and LL served as comparators.

Results: *Baseline:* FL achieved a median Dice of 0.94889 (ASSD: 1.33229), slightly better than CL at 0.94706 (ASSD: 1.37074) and LL at 0.93557–0.94026 (ASSD: 1.51910–1.69777). *Label manipulation:* FL maintained the best median Dice score at 0.94884 (ASSD: 1.46487) versus CL's 0.94183 (ASSD: 1.75738) and LL's 0.93003–0.94026 (ASSD: 1.51910–2.11462). *Image noise:* FL led with Dice at 0.94853 (ASSD: 1.31088); CL scored 0.94787 (ASSD: 1.36131); LL ranged from 0.93179–0.94026 (ASSD: 1.51910–1.77350). *Faulty-client exclusion:* FL reached Dice at 0.94790 (ASSD: 1.33113) better than CL's 0.94550 (ASSD: 1.39318). Loss-curve monitoring reliably flagged the corrupted site.

Conclusions: FL matches or exceeds CL and outperforms LL across corruption scenarios while preserving privacy. Per-client loss trajectories provide an effective anomaly-detection mechanism and support FL as a practical, privacy-preserving approach for scalable clinical AI deployment.

Key words: Federated Learning, Dental Radiography, Image Segmentation, Deep Learning, Data Heterogeneity, Flower ai, Cloud Computing.

Introduction

Artificial intelligence (AI) techniques are currently transforming and innovating diverse fields such as healthcare, finance, and logistics [1, 2]. In particular in the medical domain, AI has demonstrated considerable potential in improving diagnostic accuracy and patient treatment outcomes [3–5]. However, despite these benefits, especially for automating repetitive tasks, the integration of AI technology into clinical practice remains limited by challenges related to data collection and sharing [6–8].

The most straightforward method for training an AI model is to use locally available data, a paradigm referred to as Local Learning (LL). Yet, to achieve an optimal and generalized

model that is applicable across various hospitals, centers, and clinics (hereafter referred to as "clients"), data must ideally be aggregated in a centralized manner, which enables centralized learning (CL) [9]. This approach, however, is often restricted by regulatory, user-preference, and data volume constraints, as well as ethical and legal privacy concerns (e.g., compliance with the General Data Protection Regulation (GDPR)) [10]. Therefore, a novel approach is required that can balance high-performance model training with strict adherence to data privacy regulations.

Federated Learning (FL) offers such a solution by enabling multiple clients to collaboratively train a shared model while keeping the data on-site. Unlike a centralized approach, which would require both data and the associated computational

load to be gathered in one location, FL distributes the training workload across each data holder, making it especially attractive for medical imaging. FL allows institutions to benefit from diverse and extensive datasets without compromising patient privacy or data security [11–13]. Nevertheless, FL introduces new challenges: each client must possess adequate computational resources, a requirement that may entail significant initial economic investment, and issues related to data heterogeneity and inconsistent labeling may further complicate model performance [14]. Understanding these factors is essential to evaluate FL’s integration into medical applications and to identify elements that may either facilitate or hinder its clinical adoption.

The primary objective of this study is to investigate FL’s potential to enhance segmentation of dental anatomical structures in panoramic radiographs, while addressing some of the specific challenges associated with its implementation. To this end, we: (1) establish an FL pipeline for simulating a central server with distinct client nodes housing local data repositories; (2) Compare the performance of FL models with those trained via CL or LL; and (3) Assess the sensitivity of FL models to the variations in image quality across clients and labeling inconsistencies in order to mimic real-world scenario. Our hypothesis is that FL can significantly improve performance compared with LL and even rival the effectiveness of CL.

Data and Methods

Study Design

Panoramic radiography provides a comprehensive two-dimensional overview of the dentition and surrounding maxillofacial structures, playing a crucial role in diagnostic assessment and treatment planning [15]. While manual delineation of individual teeth is labor-intensive and subject to inter- and intra-observer variability, automated segmentation solutions provide a more standard and reliable alternative [16, 17]. This study aims to investigate the potential of FL for training neural networks to segment dental anatomical structures (i.e., teeth) in comparison to the more conventional training paradigms, namely LL and CL. To this end, we evaluate the trained models through both local validation data and centralized test data. The experiments were repeated under four conditions: (1) baseline models with unaltered data, (2) models affected by label manipulation for one client (3) models affected by image quality degradation for one client, and (4) models with one faulty client excluded. This will be discussed further in more details under the *Training procedure*.

Data

The dataset used in this study is the open-source *A dual labeled dataset* [18] (the version of the dataset was downloaded the 23rd December, 2024), that comprises of 2066 panoramic radiographs collected from three hospitals (China-Japan Union Hospital of Jilin University, Wuxi Stomatology Hospital, and People’s Hospital of Zhengzhou) and three dental clinics between January 1, 2015, and December 31, 2023. Imaging equipment was sourced from various manufacturers, including Orthophos XG (Dentsply Sirona, Germany), Planmeca ProMax (Planmeca, Finland), and Bondream 1020 (Bondream, China). The study population (989 males and 1011 females) consisted of individuals aged 16 years and older, with a mean age of 36.6 years. Data annotation was performed using Labelme

(v5.4.1) by four dentists concurrently; who delineated the teeth using polygonal annotations with zooming enabled for accuracy. Notably, dental implants were not annotated. After delineation, teeth were assigned numbering and status labels according to the Federation Dentaire Internationale (FDI) notation, ranging from 11 to 48, with 91 representing supernumerary teeth, resulting in 33 distinct numbering labels. Additionally, seven status labels were applied [18]; these are not used within the current study.

Model

We employ a U-Net with integrated attention blocks (Attention U-Net) [19] across all learning paradigms to ensure a fair evaluation. The attention U-Net was used because of its high performance in dental radiograph segmentation. As opposed to the conventional U-Net [20] that tends to process all image regions indiscriminately, the Attention U-Net incorporates attention gates to allow the model to focus on the most relevant target structures while suppressing irrelevant regions. The network architecture consists of five encoding blocks and five decoding blocks, with attention blocks integrated at the skip connections between them. Each attention gate dynamically weights the feature maps to emphasize critical anatomical details and suppress irrelevant information, via a soft attention mechanism. In brief, the concatenated feature maps are first processed by a 1×1 convolution that reduces the number of channels by a factor of eight, followed by a sigmoid activation to generate preliminary attention coefficients. A subsequent 1×1 convolution then restores the original channel dimensions, and a further sigmoid activation produces the final attention weights. These weights, which range from 0 to 1, are multiplied element-wise with the input feature map, thereby modulating the influence of each spatial region according to its relevance.

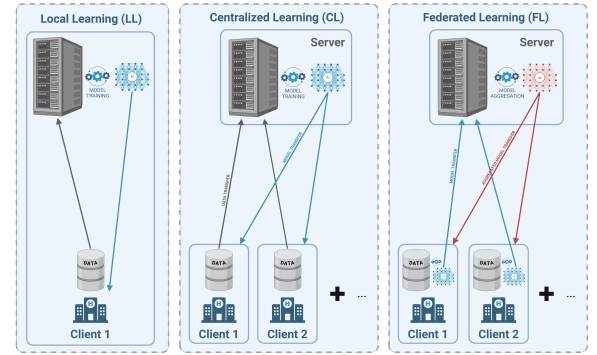


Fig. 1. Learning Paradigms, to the left Local Learning, in the middle Centralized Learning and to the right Federated Learning.

Learning Paradigms

This study investigates three learning paradigms (illustrated in Figure 1).

- **Local Learning (LL):** Training is performed solely on a single client’s local data.
- **Centralized Learning (CL):** Data from all participating clients is pooled at a central location for training, typically enhancing model’s generalizability.

- **Federated Learning (FL):** Clients do not exchange sensitive data directly but instead share model parameters, enabling joint training on diverse multi-center and multi-vendor datasets while preserving data privacy.

The proposed FL process comprises the following steps:

1. Initialize a global model on the server with random parameters.
2. Distribute the global model to the connected clients.
3. Each client trains the model locally for a predetermined number of epochs (without necessarily achieving full convergence).
4. Clients return their locally trained models to the server.
5. The server aggregates these models often using federated averaging (FedAvg) [12, 21] that computes a weighted average based on the number of training examples per client.
6. Steps 2 through 5 are repeated for several rounds until convergence, with the updated global model redistributed to all clients at the start of each round.

To implement this process, we employed Flower AI [22], an open-source framework for building federated learning pipelines.

Experimental configurations

All learning paradigms were carried out four times in different experimental configurations with the intention of investigating the performance outcome. Faulty clients were introduced as the ones whose data integrity is compromised, either through incorrect annotations or degraded image quality. Label and image quality manipulations were grounded in plausible issues that could potentially arise from a single client [23–27]. However, these manipulations were intentionally exaggerated to elicit a discernible and statistically significant response. **(1) Baseline Models:** Data remained un-altered. **(2) Label Manipulation:** To mimic poorly performed, rapid annotations, where annotators roughly trace tooth outlines rather than follow precise edges, we applied mask dilation to the ground-truth labels for one client, an example of this can be found in Figure 2. Dilation used binary kernels of size 3, 5, 7, and 11 randomly per radiograph to exaggerate boundary inaccuracy. Additionally, each image had a 10% probability of omitting one randomly selected tooth mask, simulating occasional missed annotations. **(3) Image Quality Manipulation:** For one client, image quality was degraded by adding Gaussian noise with a mean of $\mu = 0$ and a standard deviation of $\sigma = 25$ (considering an 8-bit grey scale). A configuration involving five clients was used throughout these experiments (see Figure 2 for error induced examples). **(4) Faulty Client Exclusion:** For this configuration the faulty client was excluded from participating in training the CL and FL model.

Training procedure

At first, the dataset was split with 10% (206 images and labels) randomly designated as the test set, used consistently across all paradigms and experimental configurations. Note that LL₁ through LL₄ were each trained only once, since their input data remained unchanged across configurations, whereas LL₀ was retrained for every configuration (except Faulty Client Exclusion). Data management proceeded as follows (illustrated in Figure 3):

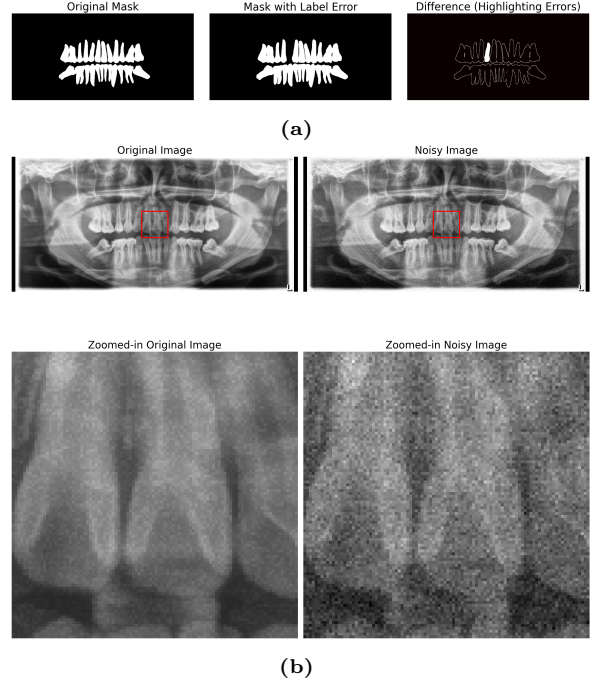


Fig. 2. Comparison between label errors and image errors. (a) Label errors in the mask, showing dilation of the label and a missing tooth. (b) Image quality degradation to one of the clients through addition of noise. Red boxes at top images act as bounding box for the bottom images.

1. Baseline models

- a. CL Models: The remaining data was partitioned into approximately 10% validation data (206 images and labels) and 80% training data (1654 images and labels).
- b. LL Models: A random sample comprising $\frac{1}{5}$ of the remaining data was made for each client and then split into approximately 10% validation data (41 images and labels) and 80% training data (331 images and labels).
- c. FL Models: An IidPartitioner was used to randomly divide (same random seed as for LL) the remaining data into five partitions, with each partition subsequently split into approximately 10% validation data (41 images and labels) and 80% training data (331 images and labels).

2. Label manipulation

- a. CL Models: Label manipulation was applied to $\frac{1}{5}$ of the remaining data, equivalent to the partition belonging to client 0, prior to splitting into validation and training sets.
- b. LL Models: Label manipulation was applied to the data belonging to client 0.
- c. FL Models: After partitioning the data into five, label manipulation was applied exclusively to the data of client 0.

3. Image manipulation

- a. CL Models: Image manipulation was applied to $\frac{1}{5}$ of the remaining data, equivalent to the partition belonging to client 0, before splitting into validation and training sets.
- b. LL Models: Image manipulation was applied to the data belonging to client 0.

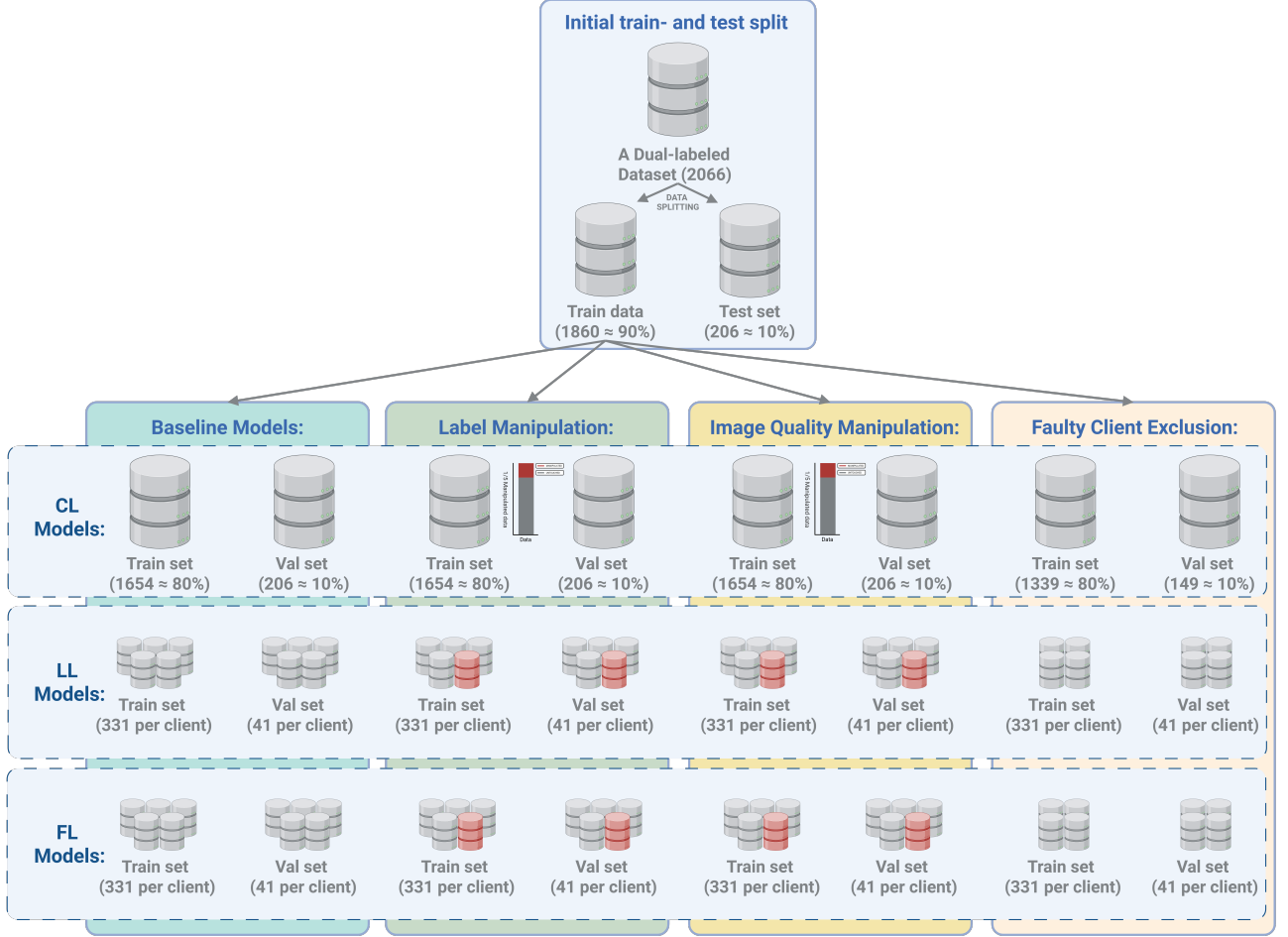


Fig. 3. Data management, showing initial split of test data, following partitioning into training (train) and validation (val) sets for each learning paradigm and experimental configuration. Grey depicts untouched data, while red shows manipulated data or labels.

- c. FL Models: After partitioning the data into five, image manipulation was applied solely to the data of client 0.

4. Faulty client exclusion

- a. CL Models: After excluding the data belonging to client 0, the remaining data was partitioned into approximately 10% validation data (149 images and labels) and 90% training data (1339 images and labels).
- b. LL Models: Same as the ones trained for baseline.
- c. FL Models: Only clients 1-4 were allowed to participate.

The most common image dimensions in the dataset were 2800×1316 pixels (aspect ratio ≈ 2.125). Prior to training, images were resized to a height of 512 pixels, with the width adjusted to 1088 pixels to preserve the aspect ratio. Images with a width smaller than 1088 pixels were zero-padded, whereas those with a larger width were cropped. Training was performed on an NVIDIA RTX 6000 Ada Generation GPU with 48 GB of graphics memory, which allowed a maximum batch size of 4 in the federated setup. The training process employed the AdamW optimizer with a learning rate of 1×10^{-4} and utilized a Dice loss function. All models were trained for 50 epochs in total; for FL models, these epochs were distributed over 5 rounds (10 epochs per round). The Flower framework was used

to simulate the federated setup, where all clients participated in the aggregation process based on FedAvg after each round, except for the Faulty Client Exclusion configuration. Tracking the training process was done using validation data after each epoch while logging metrics.

Performance metrics and statistical analysis

Model performance was evaluated primarily using Dice score (Sørensen–Dice coefficient) computed on both local validation data and the centralized test set. The Dice score quantifies the similarity between the ground truth mask G and the predicted mask P by measuring their overlap:

$$\text{Dice}(G, P) = \frac{2|G \cap P|}{|G| + |P|}, \quad (1)$$

where $|\cdot|$ denotes the number of positive pixels in a mask. The Dice score ranges from 0 (no overlap) to 1 (perfect overlap). The Dice *loss* used during training is defined as

$$\mathcal{L}_{\text{Dice}} = 1 - \text{Dice}(G, P), \quad (2)$$

and should not be confused with the Dice *score* above.

To give an extended understanding of the model performance, additional metrics were computed, including the

Intersection over Union (IoU), also known as the Jaccard index. IoU quantifies the ratio of the overlapping area to the union of the ground truth (G) and predicted (P) segmentations:

$$\text{IoU}(G, P) = \frac{|G \cap P|}{|G \cup P|} \quad (3)$$

As a complementary boundary-focused metric, the Hausdorff distance (HD) was calculated on the centralized test set. For two binary masks, the Hausdorff distance is defined as:

$$\text{HD}(G, P) = \max \left\{ \max_{g \in G} \min_{p \in P} d(g, p), \max_{p \in P} \min_{g \in G} d(p, g) \right\} \quad (4)$$

where $d(g, p)$ represents the Euclidean distance between point g in the ground truth set G and point p in the predicted segmentation set P . The 95th percentile Hausdorff distance (HD95) was also reported, which is less sensitive to outlier errors by excluding the largest 5% of point-to-point distances.

Finally, the Average Symmetric Surface Distance (ASSD) measures the mean bidirectional distance between the predicted and ground truth surfaces:

$$\text{ASSD}(G, P) = \frac{\sum_{g \in G_s} \min_{p \in P_s} d(g, p) + \sum_{p \in P_s} \min_{g \in G_s} d(p, g)}{|G_s| + |P_s|} \quad (5)$$

where G_s and P_s denote the sets of surface points in G and P , respectively. For both HD, HD95 and ASSD the distance unit is pixels, since a physical scaling factor is not applicable for this type of image.

To assess whether the metric distributions met the assumption of normality, Shapiro–Wilk tests were applied to data from each learning paradigm under every experimental configuration. As none of the groups passed the normality criterion ($p < 0.05$ for all), the analysis were conducted with non-parametric tests.

Descriptive statistics are reported as median (50th percentile), interquartile range (IQR; 25th–75th percentiles), and 95th percentile values for all metrics. To evaluate statistical significance of pairwise differences, the Wilcoxon signed-rank test (two-sided) was employed. Specifically, the following comparisons were performed:

- Within-configuration comparisons between paradigms: LL_0 vs. CL, LL_0 vs. FL, and CL vs. FL, for each of the four configurations.
- Within-paradigm comparisons across configurations: baseline vs. label manipulation, baseline vs. image quality manipulation, baseline vs. faulty client exclusion, and all other pairwise configuration combinations, for each paradigm.

To control the family-wise error rate due to multiple testing, a Bonferroni correction was applied to the significance threshold α . Adjusted $\alpha_{\text{corr}} = 0.05/N_{\text{tests}}$ was used, where N_{tests} is the total number of comparisons performed. In total, 18 tests were performed; therefore, reported p -values falling below the corrected threshold at $\alpha_{\text{corr}} = 0.00278$ were considered statistically significant.

Results

Baseline models

The training progress for each experimental configuration and its respective learning paradigms were tracked. Training progress of the baseline models can be found in Figure 4.

Metrics based on test data for all models and learning paradigms are shown in Table 1 and Figure 5. FL reached the best median score for all metrics except for HD, where CL reached a better score. LL models had the poorest performance for all metrics.

Label Manipulation

Training progress of models with induced label errors can be found in Figure 4. Note that LL models are not trained again except LL_0 , which had its data manipulated.

For each learning paradigm with induced label manipulation, FL achieved the best performance on the test data for all metrics except HD, where LL_4 scored best. CL was the second-best model, with LL models (especially LL_0 i.e. the model trained on manipulated data) generally performing the worst. Boxplots of each metric can be found in Figure 5.

Image Quality Manipulation

Training progress of models with induced image quality errors can be found in Figure 4. Note that LL models were not trained again except LL_0 which had its data manipulated.

Among the learning paradigms with induced image quality manipulation, FL exhibited the best performance on the test data for all metrics except HD, where CL reached a better score. For metrics other than HD, CL showed the second-best performance and LL models the worst, with LL_0 performing poorest. Boxplot of metrics can be found in Figure 5.

Faulty Client Exclusion

Training progress of CL and FL models excluding client 0 can be found in Figure 4; note that LL models were not trained again, since the non-excluded LL clients were already trained for the baseline configuration.

After faulty client exclusion, FL showed the best performance for all metrics except HD, where CL reached a better score. For metrics other than HD, CL showed the second-best performance, whereas LL models performed the worst. Boxplots of metrics can be found in Figure 5.

Statistical Comparison of Results

Statistical analysis using the two-sided Wilcoxon signed-rank test was performed for both within-configuration and within-paradigm comparisons. A comprehensive presentation of the significance test results can be found in Table 2 and 3 in the Appendix. Significant differences were observed across almost all configurations, with the exception of comparisons between Federated Learning (FL) and Centralized Learning (CL) based on Hausdorff Distance (HD), 95th percentile Hausdorff Distance (HD95), and Average Symmetric Surface Distance (ASSD) within the Baseline configuration; HD and HD95 within the Image Quality Manipulation configuration; and HD within the Faulty Client Exclusion configuration.

Within-paradigm comparisons revealed significant differences for all metrics when contrasting Baseline models with Label Manipulation models, except for HD in the FL model. No significant differences were detected between the Baseline and Image Quality Manipulation configurations, apart from the LL_0 model. Similarly, comparisons between Baseline and Faulty Client Exclusion models showed no statistically significant differences, although both CL and FL models demonstrated an improvement in performance when the faulty client was excluded.

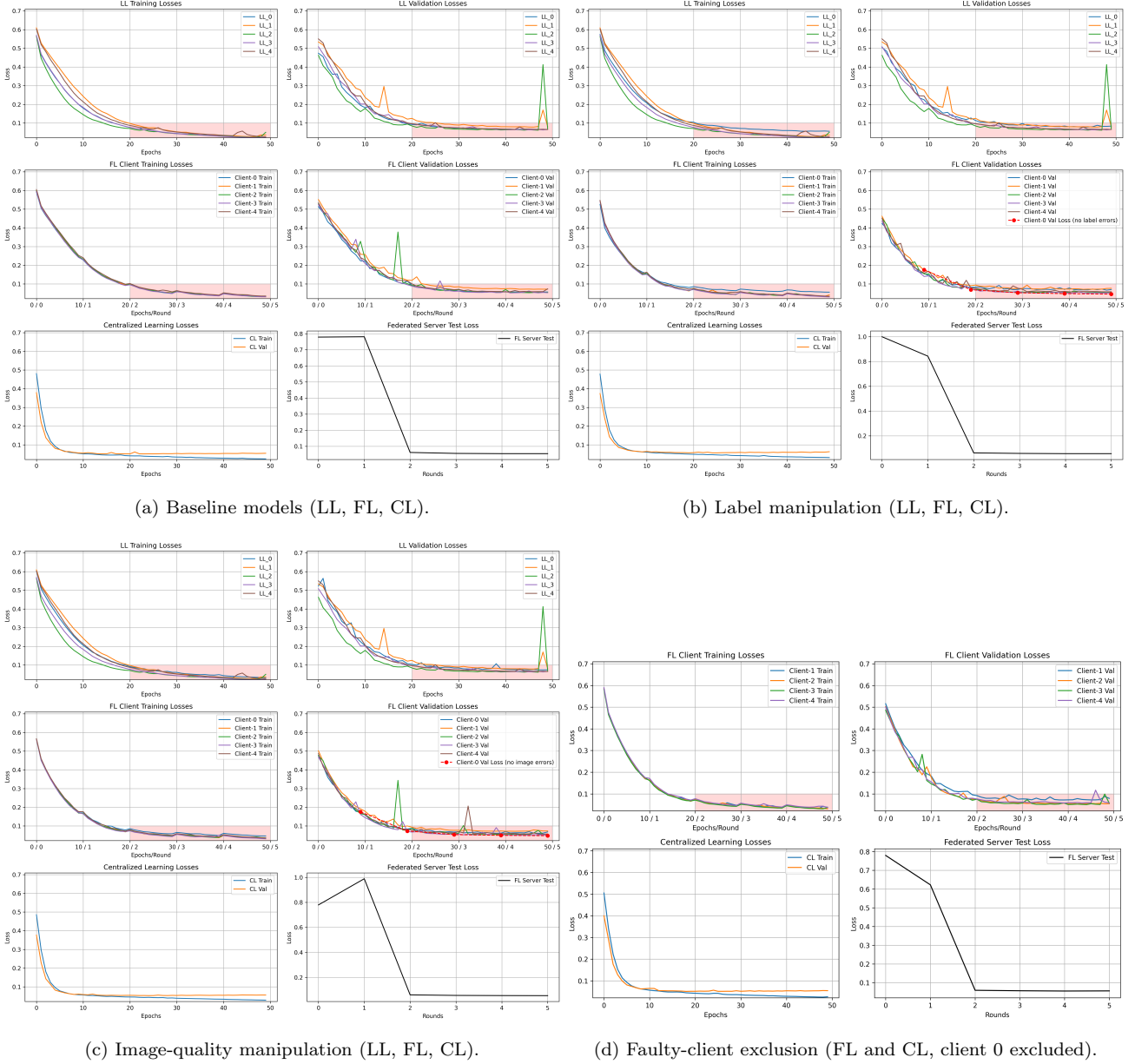


Fig. 4. Training progress for all experiments. (a) Baseline; (b) Label manipulation; (c) Image-quality manipulation; (d) Faulty-client exclusion. Red boxes indicate areas to check for convergence/elevated loss, especially for LL_0 and client-0.

Visual Comparison of Results

Representative examples for all configurations and learning paradigms are shown in Figure 6, while Figure 7 highlights the most extreme discrepancies between FL and CL. Overall, the visual comparisons indicate that CL and FL achieve highly similar segmentation performance across configurations, with small deviations found mostly in the apical regions. LL_0 consistently performs worse, mainly showing severe undersegmentation for some teeth.

The extreme case examples reveal that the largest performance gaps between CL and FL often arise in challenging cases, such as patients with sparse dentition, implants or crowns, or radiographs with artefacts. It also shows that FL errors are often spatially clustered, resulting in large contiguous false negative or false positive regions, whereas CL errors tend

to be more scattered across the image. This pattern aligns with the impression from the Dice score distributions in Figure 5, where FL shows a slightly broader spread of scores than CL, suggesting greater sensitivity to outlier cases, despite achieving comparable or higher median performance.

Discussion

A systematic evaluation of each experimental configuration and its corresponding learning paradigm yielded several notable findings. Across all training processes, no significant overfitting was detected, and the hyperparameter selection was validated as appropriate for the dataset. In Figure 4, an immediate increase in training loss following round termination was observed for FL. This phenomenon is likely attributable to

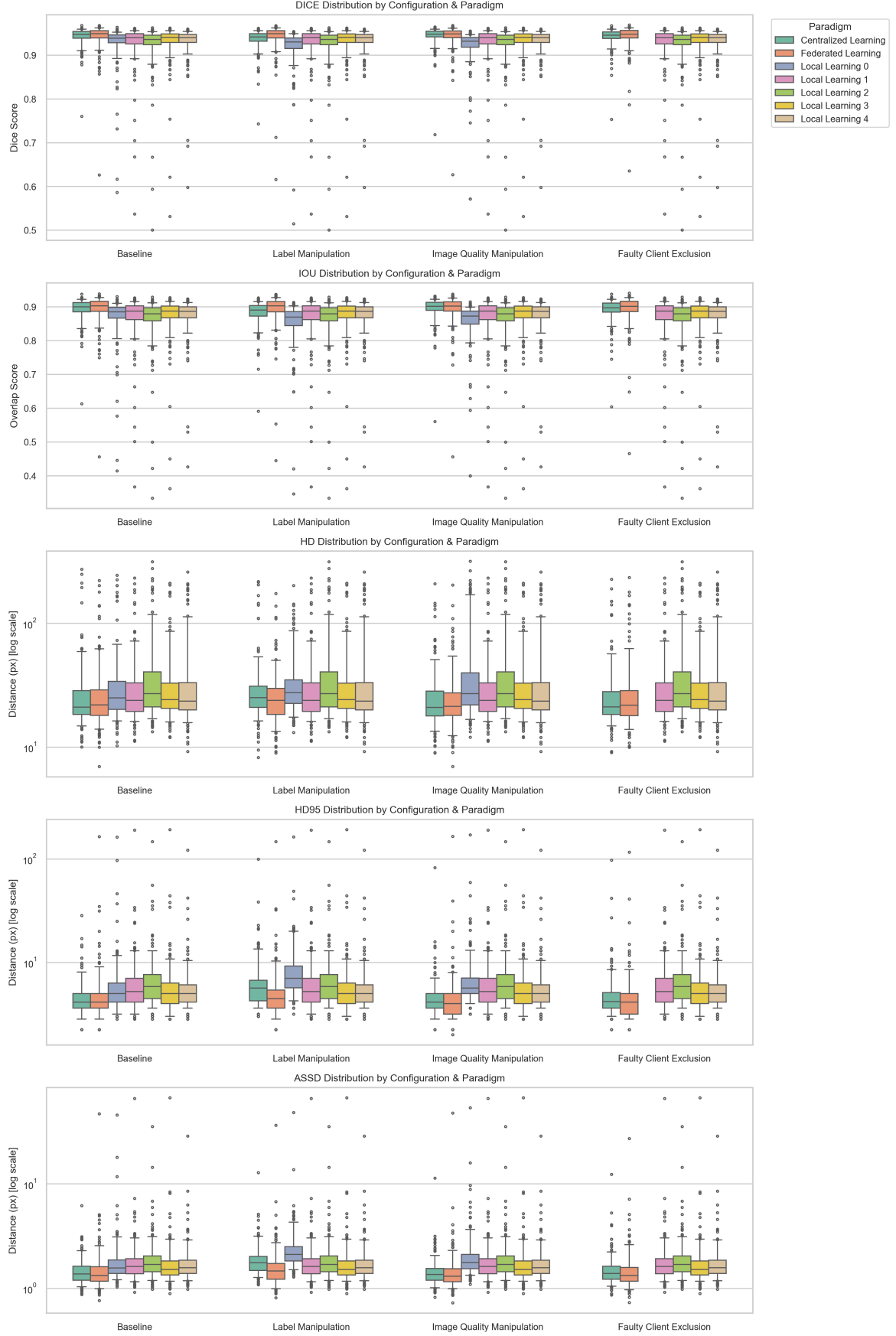
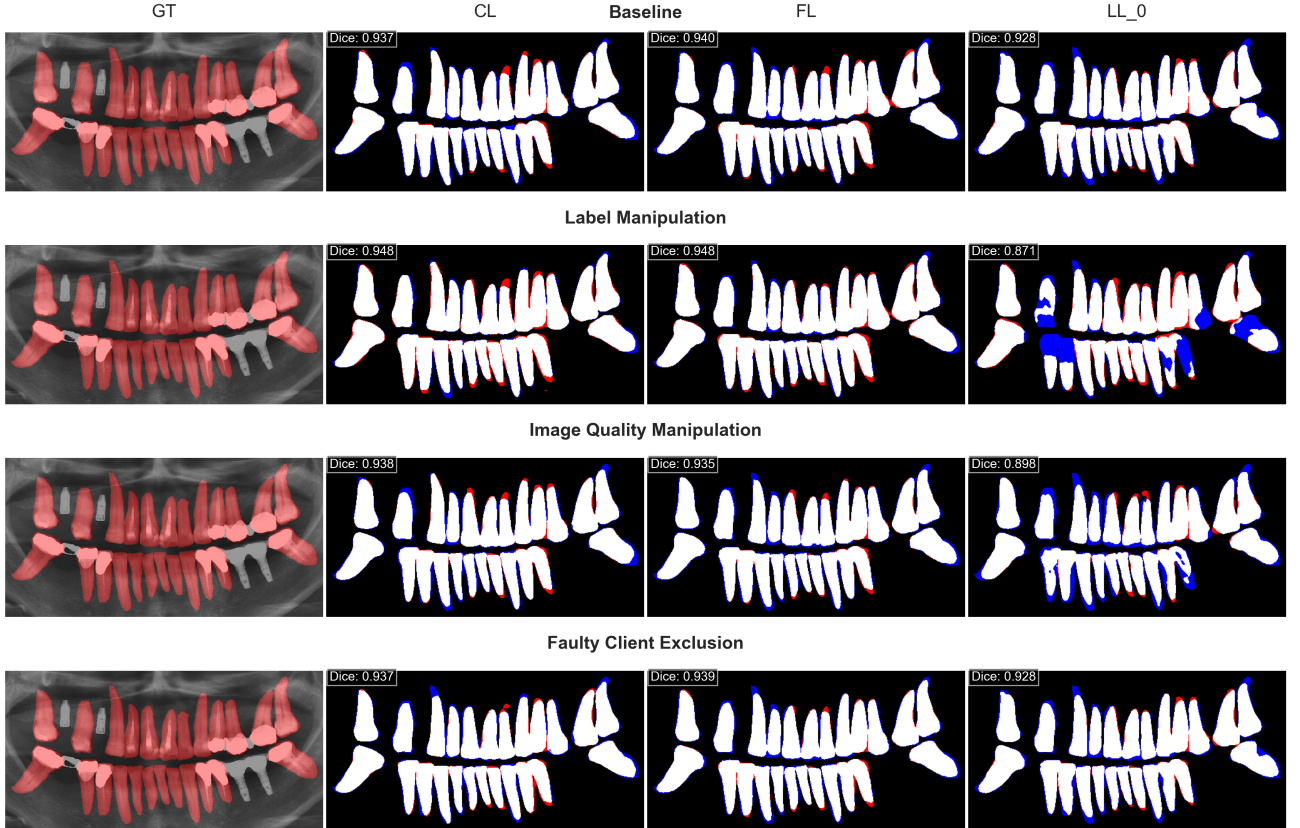


Fig. 5. Grouped boxplots with whiskers representing the [5, 95] percentiles of all metrics across centralized, federated and local learning. Outliers not within these percentiles are represented as dots.

Table 1. Descriptive statistics (Median, IQR, 95th percentile) for all metrics by Configuration and Paradigm on Test-set. The best median metric value for each configuration and metric is underlined.

Configuration	Paradigm	DICE			IOU			HD [px]			HD95 [px]			ASSD [px]		
		Median	IQR	P95	Median	IQR	P95	Median	IQR	P95	Median	IQR	P95	Median	IQR	P95
Baseline	CL	0.94706	0.01515	0.95934	0.89944	0.02730	0.92185	<u>21.09502</u>	10.20708	60.99760	<u>4.12311</u>	1.39445	8.72377	1.37074	0.43160	2.32418
	FL	<u>0.94889</u>	0.01645	0.96232	<u>0.90275</u>	0.02972	0.92737	22.00000	10.93768	62.36985	<u>4.12311</u>	1.39445	9.60976	<u>1.33229</u>	0.44289	2.62177
	LL ₀	0.93894	0.01782	0.95277	0.88491	0.03156	0.90980	25.01000	13.78110	71.53083	5.00000	2.20145	11.97776	1.56560	0.48196	3.22943
	LL ₁	0.94010	0.02327	0.95601	0.88697	0.04123	0.91572	23.89528	13.50307	73.99574	5.23494	2.87689	13.02880	1.62033	0.53646	3.13048
	LL ₂	0.93557	0.02166	0.95377	0.87895	0.03818	0.91162	27.04624	19.46147	122.04397	5.83095	3.14364	13.98837	1.69777	0.60567	3.20559
	LL ₃	0.94026	0.01981	0.95626	0.88725	0.03517	0.91618	24.19711	12.35330	87.79542	5.00000	2.32456	10.97660	1.51910	0.48987	2.96390
	LL ₄	0.93966	0.01808	0.95435	0.88619	0.03207	0.91268	23.53720	13.27045	114.15153	5.00000	1.95966	10.68782	1.57904	0.47235	2.92375
Label Manipulation	CL	0.94183	0.01717	0.95577	0.89005	0.03060	0.91529	25.12961	10.19018	57.71995	5.65685	2.46556	13.87029	1.75738	0.53663	3.17018
	FL	<u>0.94884</u>	0.01686	0.96215	<u>0.90266</u>	0.03044	0.92705	23.92686	11.44332	50.73865	<u>4.47214</u>	1.77961	10.65346	<u>1.46487</u>	0.51296	2.83928
	LL ₀	0.93003	0.02381	0.94898	0.86920	0.04140	0.90292	27.52264	12.43628	90.05001	7.00000	3.54963	20.01874	2.11462	0.68016	4.48904
	LL ₁	0.94010	0.02327	0.95601	0.88697	0.04123	0.91572	23.89528	13.50307	73.99574	5.23494	2.87689	13.02880	1.62033	0.53646	3.13048
	LL ₂	0.93557	0.02166	0.95377	0.87895	0.03818	0.91162	27.04624	19.46147	122.04397	5.83095	3.14364	13.98837	1.69777	0.60567	3.20559
	LL ₃	0.94026	0.01981	0.95626	0.88725	0.03517	0.91618	24.19711	12.35330	87.79542	5.00000	2.32456	10.97660	1.51910	0.48987	2.96390
	LL ₄	0.93966	0.01808	0.95435	0.88619	0.03207	0.91268	<u>23.53720</u>	13.27045	114.15153	5.00000	1.95966	10.68782	1.57904	0.47235	2.92375
Image Quality Manipulation	CL	0.94787	0.01317	0.95931	0.90091	0.02380	0.92181	<u>20.94031</u>	10.48371	56.05949	4.12311	1.39445	7.47960	1.36131	0.35754	2.22228
	FL	<u>0.94853</u>	0.01515	0.96145	<u>0.90210</u>	0.02736	0.92576	21.38925	9.47223	60.28257	<u>4.00000</u>	1.83772	8.04669	<u>1.31088</u>	0.39002	2.42075
	LL ₀	0.93179	0.02218	0.94702	0.87229	0.03868	0.89937	27.04624	17.87757	175.25294	5.65685	2.07107	14.19981	1.77350	0.56850	3.81118
	LL ₁	0.94010	0.02327	0.95601	0.88697	0.04123	0.91572	23.89528	13.50307	73.99574	5.23494	2.87689	13.02880	1.62033	0.53646	3.13048
	LL ₂	0.93557	0.02166	0.95377	0.87895	0.03818	0.91162	27.04624	19.46147	122.04397	5.83095	3.14364	13.98837	1.69777	0.60567	3.20559
	LL ₃	0.94026	0.01981	0.95626	0.88725	0.03517	0.91618	24.19711	12.35330	87.79542	5.00000	2.32456	10.97660	1.51910	0.48987	2.96390
	LL ₄	0.93966	0.01808	0.95435	0.88619	0.03207	0.91268	23.53720	13.27045	114.15153	5.00000	1.95966	10.68782	1.57904	0.47235	2.92375
Faulty Client Exclusion	CL	0.94550	0.01494	0.95936	0.89663	0.02688	0.92189	<u>21.14232</u>	9.73579	60.71267	4.18287	1.49347	8.57462	1.39318	0.41393	2.26050
	FL	<u>0.94790</u>	0.01694	0.96244	<u>0.90096</u>	0.03061	0.92761	21.84033	10.61997	69.72217	<u>4.12311</u>	1.83772	9.05066	<u>1.33113</u>	0.41297	2.71956
	LL ₁	0.94010	0.02327	0.95601	0.88697	0.04123	0.91572	23.89528	13.50307	73.99574	5.23494	2.87689	13.02880	1.62033	0.53646	3.13048
	LL ₂	0.93557	0.02166	0.95377	0.87895	0.03818	0.91162	27.04624	19.46147	122.04397	5.83095	3.14364	13.98837	1.69777	0.60567	3.20559
	LL ₃	0.94026	0.01981	0.95626	0.88725	0.03517	0.91618	24.19711	12.35330	87.79542	5.00000	2.32456	10.97660	1.51910	0.48987	2.96390
	LL ₄	0.93966	0.01808	0.95435	0.88619	0.03207	0.91268	23.53720	13.27045	114.15153	5.00000	1.95966	10.68782	1.57904	0.47235	2.92375

**Fig. 6.** Prediction overlays for different experimental configurations and learning paradigms. Predictions were made on the full images, with Dice scores computed before cropping. For visualization, predictions and ground truths are cropped tightly around the labeled region. Difference masks use color coding: white = true positive, red = false positive, blue = false negative, black = true negative. Only one LL client is shown, representing the 'faulty client' in scenarios involving manipulations.

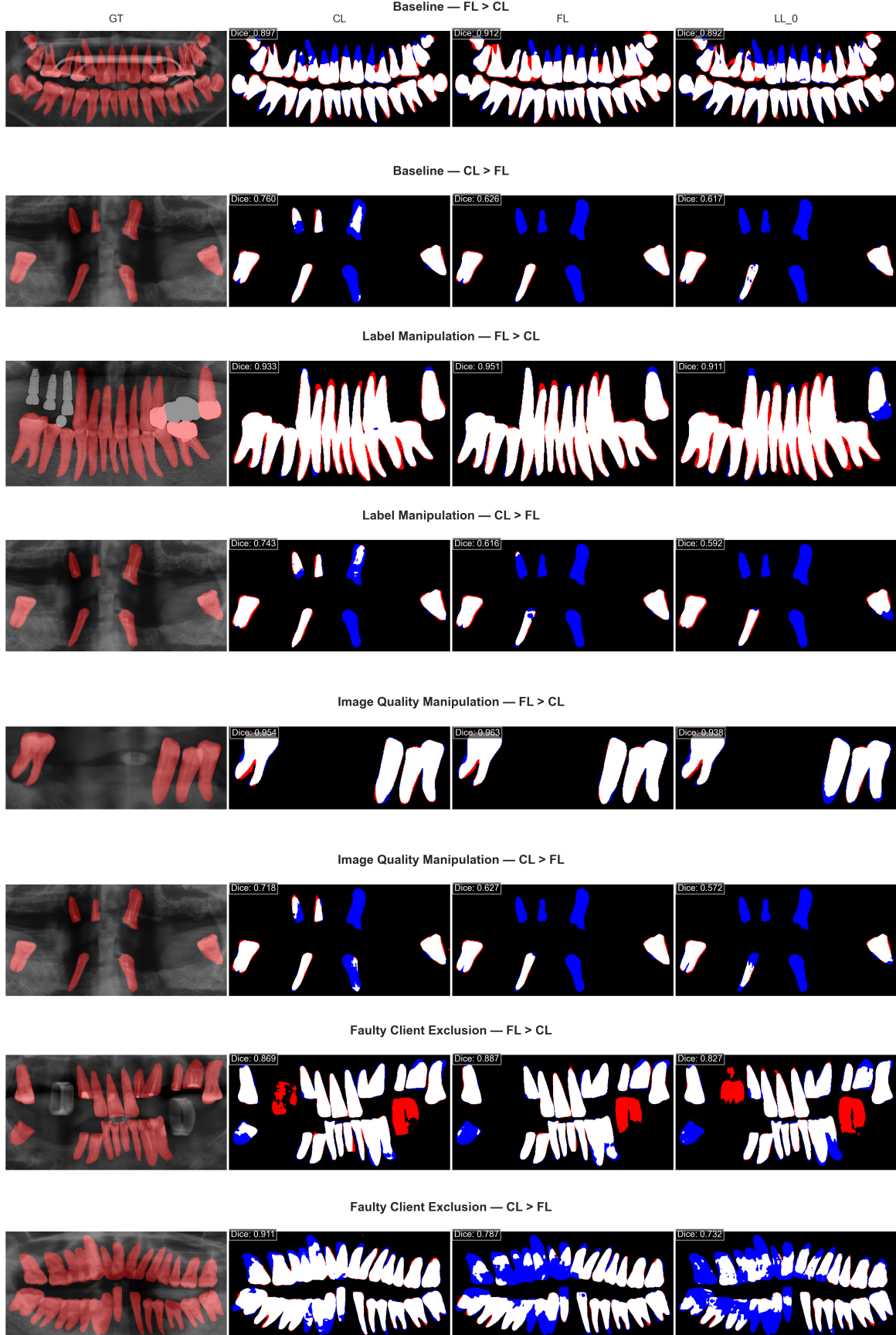


Fig. 7. Visual comparison of the most extreme segmentation cases for each configuration. For each configuration, the two most pronounced examples are shown: one where FL outperforms CL ($FL > CL$) and one where CL outperforms FL ($CL > FL$). Each row shows the ground truth (GT) with overlaid mask, followed by the difference maps for CL, FL, and the LL_0 , with corresponding Dice scores. True positives are shown in white, true negatives in black, false positives in red, and false negatives in blue.

the model aggregation process; however, the stability of the validation loss suggests that the models retained robust generalization capabilities despite the transient training loss escalation.

In terms of overall performance for the baseline models, Figure 5 demonstrates that the FL model achieved the significant highest performance, with the CL model following, and LL models exhibiting the poorest performance.

When manipulations to the labels were introduced, as illustrated in Figure 4, the faulty client (Client-0) consistently underperformed relative to the other clients. This pattern was evident in both the training loss trajectories across FL and LL paradigms. Furthermore, as shown in Figure 5, FL maintained its superior performance, followed by CL, whereas LL experienced a noticeable and significant decline in performance.

A comparable trend was observed under the image quality manipulation conditions. Figure 4 indicates that Client-0 again underperformed compared to its peers in both FL and LL settings. For this experimental configuration the FL model significantly outperformed the other learning paradigms, with CL in second place and LL in third.

We found that clients whose data had been tampered with, either via label errors or added image noise, consistently exhibited elevated training losses and slower convergence compared to their peers, highlighted in red in Figure 4. This divergence in per-client training loss trajectories can therefore act as an anomaly detector: by monitoring each client’s loss curve against the cohort distribution (for example, flagging any client whose loss exceeds the median by more than a predefined threshold), one can automatically identify and temporarily exclude “faulty” participants from the federated aggregation. Interestingly, this elevated-loss behavior does not manifest in the client’s validation-loss curves, which converge similarly to those of the other participants. Moreover, when we re-evaluate the same client on its clean validation set (i.e. without label- or image quality manipulations), the validation loss decreases noticeably (see Figure 4). In practice, these “loss-curve fingerprints” could serve as safeguards against corrupted updates. This way, the faulty client can be excluded, and a small gain in overall performance can be achieved, with FL under the Faulty Client Exclusion configuration performing slightly better than FL with label manipulation from the faulty client. While these observations are promising, the underlying cause warrants further investigation. One plausible explanation involves the use of Batch Normalization within our U-Net blocks: during training, BatchNorm layers continually update their running mean and variance to accommodate the noisy samples, leading to a higher convergence plateau in the training loss. However, during validation, in which the BatchNorm statistics are fixed, the model’s parameters remain unchanged, yielding a validation, loss trajectory that mimics that of the uncorrupted clients. Finally, when evaluated on completely clean labels, the model’s learned feature filters suppress the impact of the previously encountered noise, resulting in a lower validation loss. Overall, these “fingerprints” appear to be a combined consequence of the data corruption pattern, model architecture, and training regimen. They open the possibility of designing robust exclusion criteria to detect and mitigate under-performing clients in federated learning systems.

Most noteworthy is that FL models trained on corrupted data significantly outperformed the baseline LL models,

approximating the baseline CL models. The baseline FL model emerged as the best across all learning paradigms for all configurations. This finding suggests that the advantages inherent in a federated setup, such as improved generalization through collaborative training, can compensate for the inclusion of models trained on lower-quality data from some clients. At the same time, the increase in performance across all learning paradigms in the image-manipulated configuration suggests that the added Gaussian noise has some sort of generalizing effect, which has a confounding impact on the conclusions to be made, and relates to a completely different topic in regards of model generalizability due to data augmentation. Nevertheless, the usefulness of a federated setup is substantial and should be taken into account along with other advantages such as the distributed computational burden across multiple clients, which facilitates parallelized model training, thereby reducing overall training time. However, this approach necessitates that all clients possess adequate computational resources, specifically in terms of GPU capacity, which may impose economic constraints. Due to GPU memory limitations, a batch size of 4 was employed, although a larger batch size would generally be preferable.

Several recent studies have demonstrated the potential of federated learning in dental image analysis. Schneider et al. [11] applied FL, LL, and CL to a dataset of 4177 panoramic radiographs from nine centers, showing that FL significantly outperformed LL and approached CL performance on tooth segmentation tasks. Rischke et al. [8] further reviewed the opportunities and challenges of FL in dentistry, highlighting privacy preservation and cross-site heterogeneity as key considerations. Our results in tooth segmentation under label- and image-quality manipulation confirm these earlier findings: FL models not only surpass LL in all scenarios but also maintain robustness comparable to CL, even when some clients submit corrupted updates.

In the wider medical-imaging field, several studies have tackled annotation noise and client heterogeneity within FL. Wu et al. [28] introduced FedA3I, which weights client updates by estimated annotation quality to mitigate cross-client noise, improving segmentation performance on heterogeneous datasets. Xiang et al. [29]’s FedIA explicitly models incomplete or noisy labels across clients, as a completeness-aware aggregation weight, based on predictions from a first-stage model and its loss progression. This allows it to adjust the aggregation accordingly to the quality of data at each client. Wicaksana et al. [30]’s FedMix goes further by supporting mixed supervision levels (pixel-, box-, and image-level) in a unified FL framework, thereby enabling using different precision-level of labels for the same task, pixel-wise segmentation. Our observation, that corrupted clients can be automatically identified by their divergent training-loss trajectories and safely excluded, resonates with these quality-aware aggregation strategies and suggests a practical mechanism for enhancing FL robustness in dental and other medical imaging contexts.

The study was conducted using the Flower AI federated learning framework, which was used to simulate a distributed training environment with configurable parameters such as the number of clients, epochs training rounds, and client sampling strategies. For the present study, the standard `IidPartitioner` was employed in conjunction with `FedAvg`; however, future investigations could examine the impact of dataset heterogeneity, particularly with respect to status labels

of teeth, on FL performance [11], as well as the influence of alternative aggregation strategies (e.g., FedAdaGrad [31], FedProx [32], FedDM [33]) in combination with annotation completeness estimations. But also investigate the possibility of integration with enterprise-ready platforms such as NVFLARE to facilitate clinical implementation [34].

Conclusion

In summary, our experiments confirm that federated learning not only matches centralized learning in accuracy but also exhibits greater resilience to labeling and imaging artifacts compared to centralized learning and local learning. By monitoring per-client loss to exclude faulty participants or adjust the weighting of these, FL can further improve segmentation performance. These findings substantiate FL's potential as a practical, privacy-preserving approach for collaborative model training within the medical field.

Competing interests

No competing interest is declared.

Author contributions statement

J.R., L.E., A.I. and R.P. conceived the experiment(s), J.R. conducted the experiment(s), J.R. and R.P. analysed the results. J.R., K.N., S.J., L.E., A.I. and R.P. wrote and reviewed the manuscript.

Acknowledgments

The authors thank the anonymous reviewers for their valuable suggestions. This work was funded by: (1) the Independent Research Fund Denmark, project “Synthetic Dental Radiography using Generative Artificial Intelligence”, grant ID 10.46540/3165-00237B, for computational resources; (2) the Aarhus University Centre for Digitalisation, Big Data and Data Analytics and the Circle U Seed Funding Scheme for salary costs.

Appendix

Appendix table - Statistical Significance Tests

Table 2. Within-Configuration Wilcoxon p-values and significance (yes/no). Bonferroni-adjusted $\alpha = 0.00278$ (over 18 valid tests).

Configuration	Comparison	DICE p	DICE sig	IOU p	IOU sig	HD p	HD sig	HD95 p	HD95 sig	ASSD p	ASSD sig
Baseline	LL ₀ vs CL	4.28e-34	yes	4.04e-34	yes	4.76e-07	yes	1.68e-28	yes	6.23e-31	yes
Baseline	LL ₀ vs FL	1.02e-34	yes	9.05e-35	yes	2.74e-06	yes	2.13e-22	yes	4.79e-27	yes
Baseline	CL vs FL	3.43e-06	yes	2.91e-06	yes	8.82e-01	no	1.74e-01	no	9.52e-02	no
Label Manipulation	LL ₀ vs CL	3.12e-34	yes	2.74e-34	yes	3.62e-05	yes	1.52e-29	yes	7.76e-32	yes
Label Manipulation	LL ₀ vs FL	3.55e-34	yes	3.17e-34	yes	5.94e-14	yes	4.69e-33	yes	3.70e-33	yes
Label Manipulation	CL vs FL	3.81e-26	yes	1.96e-26	yes	3.38e-04	yes	1.04e-24	yes	4.68e-31	yes
Image Quality Manipulation	LL ₀ vs CL	1.49e-35	yes	1.49e-35	yes	3.01e-16	yes	1.42e-34	yes	7.83e-35	yes
Image Quality Manipulation	LL ₀ vs FL	1.49e-35	yes	1.49e-35	yes	4.48e-19	yes	1.66e-35	yes	1.49e-35	yes
Image Quality Manipulation	CL vs FL	1.90e-03	yes	1.85e-03	yes	2.56e-01	no	2.80e-01	no	3.60e-04	yes
Faulty Client Exclusion	CL vs FL	1.29e-10	yes	9.49e-11	yes	2.00e-01	no	2.43e-03	yes	4.00e-09	yes

Table 3. Within-Paradigm Wilcoxon p-values and significance (yes/no). Bonferroni-adjusted $\alpha = 0.00278$ (over 18 valid tests).

Paradigm	Comparison	DICE p	DICE sig	IOU p	IOU sig	HD p	HD sig	HD95 p	HD95 sig	ASSD p	ASSD sig
CL	Baseline vs Label Manipulation	9.85e-25	yes	8.63e-25	yes	3.79e-07	yes	4.48e-31	yes	7.94e-35	yes
CL	Baseline vs Image Quality Manipulation	7.34e-03	no	7.50e-03	no	2.91e-01	no	7.65e-02	no	6.22e-02	no
CL	Baseline vs Faulty Client Exclusion	3.10e-02	no	3.23e-02	no	7.63e-01	no	4.81e-05	yes	1.27e-03	yes
FL	Baseline vs Label Manipulation	3.20e-04	yes	3.47e-04	yes	4.69e-02	no	6.57e-15	yes	2.76e-18	yes
FL	Baseline vs Image Quality Manipulation	2.14e-01	no	1.90e-01	no	1.56e-01	no	4.14e-06	yes	4.06e-06	yes
FL	Baseline vs Faulty Client Exclusion	2.23e-01	no	2.15e-01	no	8.78e-01	no	4.78e-01	no	1.10e-01	no
LL ₀	Baseline vs Label Manipulation	1.09e-24	yes	1.03e-24	yes	1.52e-04	yes	1.10e-29	yes	9.88e-31	yes
LL ₀	Baseline vs Image Quality Manipulation	4.66e-28	yes	2.67e-28	yes	8.93e-05	yes	7.47e-17	yes	9.69e-24	yes

References

1. Falk Schwendicke, Tatiana Golla, Martin Dreher, and Joachim Krois. Convolutional neural networks for dental image diagnostics: A scoping review. *Journal of Dentistry*, 91:103226, 11 2019. doi: 10.1016/j.jdent.2019.103226.
2. M. I. Jordan and T. M. Mitchell. Machine learning: Trends, perspectives, and prospects. *Science*, 349(6245):255–260, 2015. doi: 10.1126/science.aaa8415. URL <https://www.science.org/doi/abs/10.1126/science.aaa8415>.
3. Hossein Mohammad-Rahimi, Saeed Reza Motamedian, Mohammad Hossein Rohban, Joachim Krois, Sergio Uribe, Erfan Nia, Rata Rokhshad, Mohadeseh Nadimi, and Falk Schwendicke. Deep learning for caries detection: A systematic review. *Journal of Dentistry*, 122:104115, 03 2022. doi: 10.1016/j.jdent.2022.104115.
4. Falk Schwendicke, Tatiana Golla, Martin Dreher, and Joachim Krois. Convolutional neural networks for dental image diagnostics: A scoping review. *Journal of Dentistry*, 91:103226, 2019. ISSN 0300-5712. doi: <https://doi.org/10.1016/j.jdent.2019.103226>. URL <https://www.sciencedirect.com/science/article/pii/S0300571219302283>.
5. Shuroug Alowais, Sahar Alghamdi, Nada Alsuehany, Tariq Alqahtani, Abdulrahman Alshaya, Sumaya Almohareb, Atheer Aldairem, Mohammed Alrashed, Khalid Saleh, Hisham Badreldin, Majed Al Yami, Shmeylan Al Harbi, and Abdulkareem Albekairy. Revolutionizing healthcare: the role of artificial intelligence in clinical practice. *BMC Medical Education*, 23, 09 2023. doi: 10.1186/s12909-023-04698-z.
6. Nicola Rieke, Jonny Hancox, Wenqi Li, Fausto Milletari, Holger Roth, Shadi Albarqouni, Spyridon Bakas, Mathieu Galtier, Bennett Landman, Klaus Maier-Hein, Sébastien Ourselin, Micah Sheller, Ronald Summers, Andrew Trask, Daguang Xu, Maximilian Baust, and Manuel Jorge Cardoso. The future of digital health with federated learning. *npj Digital Medicine*, 3, 12 2020. doi: 10.1038/s41746-020-00323-1.
7. Erfan Darzi, Mohammad Ghasemi-rad, and P.m.a Ooijen. Federated learning in medical imaging: Part ii: Methods, challenges, and considerations. *Journal of the American College of Radiology*, 19, 04 2022. doi: 10.1016/j.jacr.2022.03.016.
8. R. Rischke, Lisa Schneider, K. Müller, Wojciech Samek, Falk Schwendicke, and Joachim Krois. Federated learning in dentistry: Chances and challenges. *Journal of Dental Research*, 101:002203452211089, 07 2022. doi: 10.1177/00220345221108953.
9. Joachim Krois, Anselmo Cantu, Akhilanand Chaurasia, Ranjitkumar Patil, Prabhat Chaudhari, Robert Gaudin, Sascha Gehrung, and Falk Schwendicke. Generalizability of deep learning models for dental image analysis. *Scientific Reports*, 11:6102, 03 2021. doi: 10.1038/s41598-021-85454-5.
10. Paul Voigt and Axel Bussche. *The EU General Data Protection Regulation (GDPR): A Practical Guide*. 01 2017. ISBN 978-3-319-57958-0. doi: 10.1007/978-3-319-57959-7.
11. Federated vs local vs central deep learning of tooth segmentation on panoramic radiographs. *Journal of Dentistry*, 135:104556, 2023. ISSN 0300-5712. doi: <https://doi.org/10.1016/j.jdent.2023.104556>.
12. Brendan McMahan, Eider Moore, Daniel Ramage, Seth Hampson, and Blaise Aguera y Arcas. Communication-efficient learning of deep networks from decentralized data. In *Artificial intelligence and statistics*, pages 1273–1282. PMLR, 2017.
13. Tian Li, Anit Kumar Sahu, Ameet Talwalkar, and Virginia Smith. Federated learning: Challenges, methods, and future directions. *IEEE signal processing magazine*, 37(3):50–60, 2020.
14. Mahdi Morafah, Saeed Vahidian, Chen Chen, Mubarak Shah, and Bill Lin. Rethinking data heterogeneity in federated learning: Introducing a new notion and standard benchmarks. *arXiv preprint arXiv:2209.15595*, 2022.
15. Rossana Izzetti, Marco Nisi, Giacomo Aringhieri, Laura Crocetti, Filippo Graziani, and Cosimo Nardi. Basic knowledge and new advances in panoramic radiography imaging techniques: A narrative review on what dentists and radiologists should know. *Applied Sciences*, 11, 08 2021. doi: 10.3390/app11177858.
16. Jayasankar Pillai, Debesh Nilendu, Namitha Thomas, Sugandha Nagpal, and Sneha Nedunari. Inter-observer agreement in the radiographic interpretation of demirjian’s developmental stages in the mandibular second and third molars -a comparative study. *Journal of Oral and Maxillofacial Pathology*, 25:554, 01 2022. doi: 10.4103/jomfp.jomfp-85-21.
17. M. Bonfanti-Gris, Ángel Herrera, María Salido, Francisco Martínez-Rus, and Guillermo Pradies. Deep learning for tooth detection and segmentation in panoramic radiographs: a systematic review and meta-analysis. *BMC Oral Health*, 25, 07 2025. doi: 10.1186/s12903-025-06349-9.
18. Wenbo Zhou, Xin Lu, Dan Zhao, Meng Jiang, Linlin Fan, Weihang Zhang, Fenglin Li, Dezhou Wang, Weihuang Yin, and Xin Liu. A dual-labeled dataset and fusion model for automatic teeth segmentation, numbering, and state assessment on panoramic radiographs. *BMC Oral Health*, 24, 10 2024. doi: 10.1186/s12903-024-04984-2.
19. Dishant Padalia, Kush Vora, and Deepak Sharma. An attention u-net for semantic segmentation of dental panoramic x-ray images. In *2022 5th International Conference on Advances in Science and Technology (ICAST)*, pages 491–496, 2022. doi: 10.1109/ICAST55766.2022.10039666.
20. Olaf Ronneberger, Philipp Fischer, and Thomas Brox. U-net: Convolutional networks for biomedical image segmentation. In *Medical image computing and computer-assisted intervention—MICCAI 2015: 18th international conference, Munich, Germany, October 5–9, 2015, proceedings, part III* 18, pages 234–241. Springer, 2015.
21. Jakub Konečný, Brendan McMahan, and Daniel Ramage. Federated optimization: distributed optimization beyond the datacenter. 11 2015. doi: 10.48550/arXiv.1511.03575.
22. flower.ai. What is federated learning?, 2025. URL <https://flower.ai/docs/framework/tutorial-series-what-is-federated-learning.html>. Accessed on 04/03, 2025.
23. Martha Büttner, Lisa Schneider, Aleksander Krasowski, Joachim Krois, Ben Feldberg, and Falk Schwendicke. Impact of noisy labels on dental deep learning—calculus detection on bitewing radiographs. *Journal of Clinical Medicine*, 12:3058, 04 2023. doi: 10.3390/jcm12093058.
24. Ayetullah Güneş, Ward Rooij, Sadaf Gulshad, Berend Slotman, Max Dahele, and Wilko Verbakel. Impact of

- imperfection in medical imaging data on deep learning-based segmentation performance: An experimental study using synthesized data. *Medical Physics*, 50, 04 2023. doi: 10.1002/mp.16437.
25. Hak-Sun Kim, Eun-Gyu Ha, Ari Lee, Yoon Joo Choi, Kug Jeon, Sang-Sun Han, and Chena Lee. Refinement of image quality in panoramic radiography using a generative adversarial network. *Dentomaxillofacial Radiology*, 52, 05 2023. doi: 10.1259/dmfr.20230007.
 26. Peter Goebel, A.N. Belbachir, and Michael Truppe. Noise estimation in panoramic x-ray images: an application analysis approach. pages 996 – 1001, 08 2005. doi: 10.1109/SSP.2005.1628740.
 27. Songyue Lin, Xuejiang Hao, Yan Liu, Dong Yan, Jianwei Liu, and Mingjun Zhong. Lightweight deep learning methods for panoramic dental x-ray image segmentation. *Neural Computing and Applications*, 35:1–12, 12 2022. doi: 10.1007/s00521-022-08102-7.
 28. Nannan Wu, Zhaobin Sun, Zengqiang Yan, and Meiqi Li. Fed3i: Annotation quality-aware aggregation for federated medical image segmentation against heterogeneous annotation noise. *Proceedings of the AAAI Conference on Artificial Intelligence*, 38:15943–15951, 03 2024. doi: 10.1609/aaai.v38i14.29525.
 29. Yangyang Xiang, Nannan Wu, Meiqi Li, Kwang-Ting Cheng, and Zengqiang Yan. *FedIA: Federated Medical Image Segmentation with Heterogeneous Annotation Completeness*, pages 373–382. 10 2024. ISBN 978-3-031-72116-8. doi: 10.1007/978-3-031-72117-5_35.
 30. Jeffry Wicaksana, Zengqiang Yan, Dong Zhang, Xijie Huang, Huimin Wu, and K.-T. Tim Cheng. Fedmix: Mixed supervised federated learning for medical image segmentation. *IEEE Transactions on Medical Imaging*, PP:1–1, 12 2022. doi: 10.1109/TMI.2022.3233405.
 31. Sashank J. Reddi, Zachary Charles, Manzil Zaheer, Zachary Garrett, Keith Rush, Jakub Konečný, Sanjiv Kumar, and H. McMahan. Adaptive federated optimization, 02 2020.
 32. Tian Li, Manzil Zaheer, Maziar Sanjabi, Ameet Talwalkar, and Virginia Smith. Federated optimization for heterogeneous networks, 01 2019.
 33. Yuanhao Xiong, Ruochen Wang, Minhao Cheng, Felix Yu, and Cho-Jui Hsieh. Feddm: Iterative distribution matching for communication-efficient federated learning, 07 2022.
 34. Holger Roth, Daniel Beutel, Yan Cheng, Javier Marques, Heng Pan, Chester Chen, Zhihong Zhang, Yuhong Wen, Sean Yang, Isaac Yang, Yuan-Ting Hsieh, Ziyue Xu, Daguang Xu, Nicholas Lane, and Andrew Feng. *Supercharging Federated Learning with Flower and NVIDIA FLARE*, pages 36–45. 03 2025. ISBN 978-3-031-82239-1. doi: 10.1007/978-3-031-82240-7_3.



Johan Andreas Balle Rubak. Biomedical Engineering student at Aarhus University and Research Assistant in the Department of Dentistry and Oral Health. I hold a deep interest in medical image modalities, 3D-modelling tools for clinical workflows and how to enable AI within these field, in particularly with federated learning.